Growing skin: A computational model for skin expansion in reconstructive surgery

Adrián Buganza Tepole [a], Christopher Joseph Ploch [a], Jonathan Wong [a], Arun K. Gosain [b], Ellen Kuhl [a,c,d,*]

[a] Department of Mechanical Engineering, Stanford University, Stanford, CA 94305, USA
[b] Department of Plastic Surgery, Rainbow Babies and Children's Hospital, Case Western Reserve University, Cleveland, OH 44106, USA
[c] Department of Bioengineering, Stanford University, Stanford, CA 94305, USA
[d] Department of Cardiothoracic Surgery, Stanford University, Stanford, CA 94305, USA

ARTICLE INFO

ABSTRACT

The goal of this manuscript is to establish a novel computational model for stretch-induced skin growth during tissue expansion. Tissue expansion is a common surgical procedure to grow extra skin for reconstructing birth defects, burn injuries, or cancerous breasts. To model skin growth within the framework of nonlinear continuum mechanics, we adopt the multiplicative decomposition of the deformation gradient into an elastic and a growth part. Within this concept, we characterize growth as an irreversible, stretch-driven, transversely isotropic process parameterized in terms of a single scalar-valued growth multiplier, the in-plane area growth. To discretize its evolution in time, we apply an unconditionally stable, implicit Euler backward scheme. To discretize it in space, we utilize the finite element method. For maximum algorithmic efficiency and optimal convergence, we suggest an inner Newton iteration to locally update the growth multiplier at each integration point. This iteration is embedded within an outer Newton iteration to globally update the deformation at each finite element node. To demonstrate the characteristic features of skin growth, we simulate the process of gradual tissue expander inflation. To visualize growth-induced residual stresses, we simulate a subsequent tissue expander deflation. In particular, we compare the spatio-temporal evolution of area growth, elastic strains, and residual stresses for four commonly available tissue expander geometries. We believe that predictive computational modeling can open new avenues in reconstructive surgery to rationalize and standardize clinical process parameters such as expander geometry, expander size, expander placement, and inflation timing.

1. Motivation

Tissue expansion has revolutionized reconstructive surgery in the last three decades. It was first proposed more than half a century ago to reconstruct a traumatic ear defect using a temporarily implanted rubber balloon (Neumann, 1959). However, the technique was rarely used in clinical practice until it was rediscovered over 20 years later as an option for

* Corresponding author at: Department of Mechanical Engineering, Stanford University, 496 Lomita Mall, Stanford, CA 94305, USA.
Tel.: +1 650 450 0855; fax: +1 650 725 1587.
E-mail addresses: abuganza@stanford.edu (A.B. Tepole), cploch@stanford.edu (C.J. Ploch), jonjwong@stanford.edu (J. Wong), arun.gosain@uhhospitals.org (A.K. Gosain), ekuhl@stanford.edu (E. Kuhl).
URL: http://biomechanics.stanford.edu (E. Kuhl).

Fig. 1. Tissue expansion for pediatric forehead reconstruction. The patient, a one-year old girl, presented with a giant congenital nevus involving almost 50% of the forehead, affecting the hairline and the left eyebrow. Three forehead and scalp expanders were implanted simultaneously for in situ forehead flap growth. For complete resurfacing of the region, serial tissue expansion was performed to successively stretch the previously expanded tissues until the entire nevus could be excised and resurfaced. This technique allows to resurface large anatomical areas with skin of similar color, quality, and texture. The follow-up photograph shows the patient at age three; the initial defect was excised and resurfaced with expanded forehead and scalp flaps.

skin expansion in post-mastectomy breast reconstruction (Radovan, 1982). Since then, application of tissue expansion for breast reconstruction has gained widespread use. The technique has since advanced as one of the key surgical procedures to create skin flaps for the resurfacing of large congenital defects of the skin including giant nevi and vascular anomalies (Arneja and Gosain, 2007, 2009; Gosain et al., 2001). It is also widely used for the correction of skin deformity following burn injuries and other forms of traumatic skin loss (Argenta et al., 1983; Das and Gosain, 2009). Skin expansion is an ideal way to grow skin that matches the color, texture, and hair bearance of the surrounding healthy skin, while minimizing scars and risk of rejection (Rivera et al., 2005). Fig. 1 illustrates an example of tissue expansion in pediatric forehead reconstruction (Gosain et al., 2009). The patient, a one-year old girl, presented with a giant congenital nevus involving almost 50% of the forehead, affecting the hairline and the left eyebrow. Three forehead and scalp expanders were used simultaneously for in situ forehead flap growth. For complete resurfacing of the region, serial tissue expansion was then performed, successively stretching the previously expanded tissues until the entire nevus could be excised and resurfaced. In skin resurfacing, tissue expanders are typically placed in subcutaneous pockets adjacent to the skin defect, while their ports to regulate expander filling are either buried in a remote location away from the defect, or left outside the skin for ease of injection. The amount of filling is controlled by visual inspection of skin color, capillary refill, and simple palpation of the skin over the expander (Rivera et al., 2005). Multiple subsequent serial inflations stretch the skin and stimulate tissue growth. Once new skin is produced, the device is removed, and the new skin is used to repair the adjacent defect zone. The follow-up photograph in Fig. 1, right, shows the patient at age three after the initial defect was excised and resurfaced with expanded forehead and scalp flaps. Similar expansion techniques have successfully been used to grow skin in the trunk (Arneja and Gosain, 2005), and in the upper and lower extremities (Gosain et al., 2001).

Fig. 2 shows a schematic sequence of the mechanical processes that occur during tissue expansion. Initially, at biological equilibrium, the skin is in a natural state of resting tension (Silver et al., 2003). Skin is a composite material consisting of two layers: the epidermis, a 0.06–1.0 mm thick waterproof, protective outer layer and the dermis, a 1.0–4.0 mm thick load bearing inner layer (Silver et al., 2003). When used for skin resurfacing, tissue expanders are implanted in the subcutaneous tissue beneath these two skin layers. When the expander is inflated, the epidermis and the dermis are loaded in tension. Dermal stretches beyond a critical level trigger a series of stretch-induced signaling
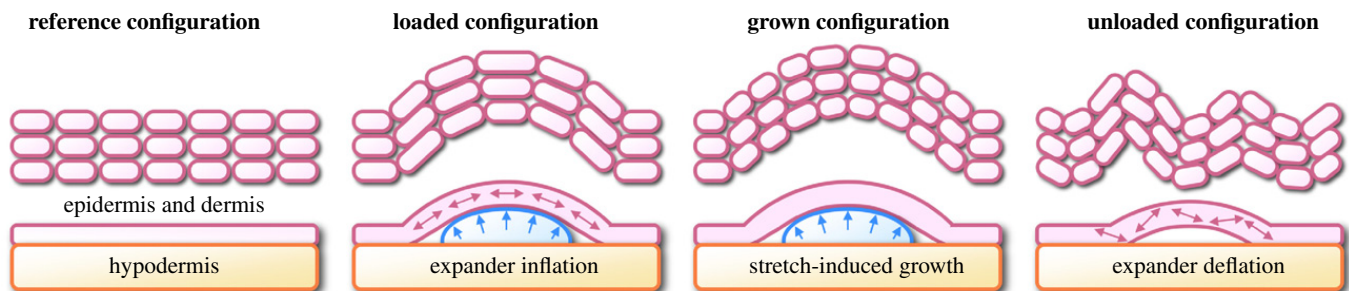
Fig. 2. Schematic sequence of tissue expander inflation and deflation. At biological equilibrium, the skin is in a physiological state of resting tension, left. A tissue expander is implanted subcutaneously between the skin, consisting of the epidermis and dermis, and the hypodermis. When the expander is inflated, the skin is loaded in tension, middle left. Mechanical stretch induces cell proliferation causing the skin to grow. Growth restores the state of resting tension, middle right. Expander deflation reveals the irreversible nature of skin growth associated with growth-induced residual stresses in the skin layer, right.

pathways (Takei et al., 1998). Mechanotransduction affects a network of integrated cascades including cellular architecture and function such as cytoskeletal structure, extracellular matrix, enzyme activity, second messenger systems, and ion channel activity (De Filippo and Atala, 2002). As a consequence, the skin grows and restores the state of resting tension. This cycle of expander inflation and growth is repeated multiple times, typically on a weekly basis. Remarkably, as demonstrated by immunocytochemical analyses, the expanded tissue undergoes normal cell differentiation and maintains its characteristic phenotype (Wollina et al., 1992). When the expander is removed, the skin retracts and reveals the irreversible nature of skin growth. This is associated with growth-induced residual stresses in the skin layer (Goriely and BenAmar, 2005). Although the tissue initially displays epidermal thickening and dermal thinning upon expansion, both thickness changes are reversible under expander removal (van der Kolk et al., 1987).

Several studies have focused on understanding this adaptation process from a biomechanical point of view. In this endeavor, two parameters have received special attention: the rate of expansion and the expander geometry. A series of in vivo experiments has demonstrated that the rate of expansion, every day over a period of two weeks versus weekly over a period of six weeks, had no significant impact on area gain and biomechanical tissue properties (Zeng et al., 2003). The expander geometry, however, seems to play a more crucial role (Brobmann and Huber, 1985). Fig. 3 displays four commonly used tissue expander geometries, circular, square, rectangular, and crescent-shaped. For regular circular and rectangular expanders, simple mathematical models have been proposed to kinematically correlate expander volume and surface area (Duits et al., 1989; Shively, 1986). However, it was soon recognized that purely kinematic models severely overestimate the net gain in surface area (van Rappard et al., 1988). The observed difference of up to a factor four seems obvious, since these models assume that the entire deformation can be attributed to irreversible growth, completely neglecting the reversible elastic deformation that manifests itself in skin retraction upon expander removal (LoGiudice and Gosain, 2003), see Fig. 2, right. To correct for this error, empirical correction factors of 6.0, 3.75, and 4.5 have been proposed for the circular, rectangular, and crescent-shaped expanders (van Rappard et al., 1988). Despite these efforts, the choice of the appropriate expander geometry and size is still almost exclusively based on the surgeon's personal preference, and the discrepancy between recommended shapes, sizes, and volumes remains enormous (LoGiudice and Gosain, 2003). This demonstrates the ongoing need to rationalize criteria for a standardized device selection.

In this paper, we propose a rigorous, mechanistic approach to systematically compare different tissue expander geometries in terms of stress, strain, and area gain. To model skin growth in response to tissue expansion, we adopt the framework of finite growth. Finite growth theories have experienced a breakthrough in continuum thermodynamics with the introduction of an incompatible growth configuration, along with the corresponding multiplicative decomposition of the deformation gradient into an elastic and a growth part (Rodriguez et al., 1994). This idea is not new. Its basic concept was originally developed in the context of finite strain plasticity (Lee, 1969), and was then adopted for biological growth (Taber, 1995). Today, there seems to be a general agreement that the incompatible growth configuration is a suitable and effective approach towards finite growth, and a tremendous amount of research has been devoted to establish continuum theories of finite growth within the last decade (Dunlop et al., 2010; Epstein and Maugin, 2000; Goriely and BenAmar, 2007; Lubarda and Hoger, 2002). These theories have been applied successfully to characterize growing tumors (Ambrosi and Mollica, 2002; Dervaux and Ben Amar, 2011), tendons (Garikipati et al., 2004), mucous membranes (Moulton and Goriely, 2011; Li et al., 2011), vascular tissues (Humphrey, 2002; Kuhl et al., 2007; Taber and Humphrey, 2001), and cardiac tissues (Göktepe et al., 2010a; Kroon et al., 2009; Rausch et al., in press). While earlier studies were primarily of theoretical and analytical nature (Ben Amar and Goriely, 2005; Ganghoffer, 2010; Garikipati, 2009), we can now observe a clear trend towards the computational modeling of volumetric growth, typically by introducing the growth tensor as an internal variable within a finite element framework (Göktepe et al., 2010b; Himpel et al., 2005; Schmid et al., in press). A recent monograph summarizes the essential findings, trends, and open questions in this progressively evolving new field (Ambrosi et al., 2011).

Despite ongoing research in growing biological systems, the growth of thin biological membranes remains severely understudied. Only recently, first attempts have been presented to mathematically characterize growth-induced

Fig. 3. Tissue expanders to grow skin flaps for defect correction in reconstructive surgery. Typical applications are birth defect correction, scar revision in burn injuries, and breast reconstruction after tumor removal. Devices are available in different shapes and sizes, circular, square, rectangular, and crescent-shaped. They consist of a silicone elastomer inflatable expander with a reinforced base for directional expansion, and a remote silicone elastomer injection dome. Reprinted with permission, Mentor Worldwide LLC.

instabilities and residual stresses in thin elastic membranes (Dervaux et al., 2009; Goriely and BenAmar, 2005; McMahon and Goriely, 2010). However, despite a few exceptions (Li et al., 2011), most of these attempts remain restricted to an axisymmetric response. Unfortunately, the same is true for the only computational model for skin growth proposed to date (Socci et al., 2007), which is unsuitable to model arbitrary tissue expander geometries. It is of axisymmetric nature and can therefore only be applied to model skin growth using a circular tissue expander. The promising first results of this study have motivated our attempts to create a fully three-dimensional computational model for tissue expansion that allows us to precisely quantify stress, strain, and area gain in response to different, arbitrarily shaped tissue expander geometries.

To document our efforts, this paper is organized as follows. In Section 2, we give a brief overview of the continuum equations for finite growth including the kinematic equations, the balance equations, and the constitutive equations. In particular, we introduce the growth tensor for transversely isotropic growth and the strain-driven evolution equation for its key kinematic variable, the area growth. In Section 3, we illustrate the temporal and spatial discretizations of the biological and mechanical equilibrium equations, along with their consistent algorithmic linearization. We then demonstrate the features of our model in Section 4, focussing on the two load cases of tissue expander inflation and deflation. After pointing out the limitations of our model, we close with some concluding remarks in Section 5.

2. Continuum modeling of area growth

In this section, we introduce the governing equations of area growth within the framework of open system thermodynamics. We briefly summarize the kinematic equations, the balance equations, and the constitutive equations.

2.1. Kinematics of area growth

We adopt the kinematics of finite deformations and introduce the deformation map $\boldsymbol{\varphi}$, which, at any given time t, maps the material placement $\boldsymbol{X}$ of a physical particle in the material configuration to its spatial placement $\boldsymbol{x}$ in the spatial configuration:

$$\boldsymbol{x} = \boldsymbol{\varphi}(\boldsymbol{X}, t) \tag{1}$$

In what follows, we apply a formulation which is entirely related to the material frame of reference. Accordingly, $\nabla\{\circ\} = \partial_{\boldsymbol{X}}\{\circ\}|_t$ and $\mathrm{Div}\{\circ\} = \partial_{\boldsymbol{X}}\{\circ\}|_t : \boldsymbol{I}$ denote the gradient and the divergence of any field $\{\circ\}(\boldsymbol{X}, t)$ with respect to the material placement $\boldsymbol{X}$ at fixed time t. Herein $\boldsymbol{I}$ is the material identity tensor. To characterize finite growth, we adopt the multiplicative decomposition of deformation gradient

$$\boldsymbol{F} = \boldsymbol{F}^{\mathrm{e}} \cdot \boldsymbol{F}^{\mathrm{g}} \quad \text{with } \boldsymbol{F} = \nabla_{\boldsymbol{X}} \boldsymbol{\varphi} \tag{2}$$

into an elastic part $\boldsymbol{F}^{\mathrm{e}}$ and a growth part $\boldsymbol{F}^{\mathrm{g}}$ (Rodriguez et al., 1994). This implies that the total Jacobian

$$J = J^{\mathrm{e}} J^{\mathrm{g}} \quad \text{with } J = \det(\boldsymbol{F}) > 0 \tag{3}$$

obeys a similar multiplicative decomposition into an elastic part $J^{\mathrm{e}} = \det(\boldsymbol{F}^{\mathrm{e}})$ and a growth part $J^{\mathrm{g}} = \det(\boldsymbol{F}^{\mathrm{g}})$. We idealize skin as a thin layer characterized through the unit normal $\boldsymbol{n}_0$ in the undeformed reference configuration. The length of the deformed skin normal $\boldsymbol{n} = \mathrm{cof}(\boldsymbol{F}) \cdot \boldsymbol{n}_0 = J\,\boldsymbol{F}^{-\mathrm{t}} \cdot \boldsymbol{n}_0$ introduces the area stretch

$$\vartheta = \vartheta^{\mathrm{e}} \vartheta^{\mathrm{g}} \quad \text{with } \vartheta = \|\mathrm{cof}(\boldsymbol{F}) \cdot \boldsymbol{n}_0\| = J[\boldsymbol{n}_0 \cdot \boldsymbol{C}^{-1} \cdot \boldsymbol{n}_0]^{1/2} \tag{4}$$

which we can again decompose into an elastic area stretch $\vartheta^{\mathrm{e}} = \|\mathrm{cof}(\boldsymbol{F}^{\mathrm{e}}) \cdot \boldsymbol{n}_g\|$ and a growth area stretch $\vartheta^{\mathrm{g}} = \|\mathrm{cof}(\boldsymbol{F}^{\mathrm{g}}) \cdot \boldsymbol{n}_0\|$. Here, $\mathrm{cof}(\circ) = \det(\circ)(\circ)^{-\mathrm{t}}$ denotes the cofactor of the second order tensor $(\circ)$. As characteristic deformation measures, we introduce the right Cauchy Green tensor $\boldsymbol{C}$ in the undeformed reference configuration and its elastic counterpart $\boldsymbol{C}^{\mathrm{e}}$ in the intermediate configuration,

$$\boldsymbol{C} = \boldsymbol{F}^{\mathrm{t}} \cdot \boldsymbol{F} \quad \text{and } \boldsymbol{C}^{\mathrm{e}} = \boldsymbol{F}^{\mathrm{et}} \cdot \boldsymbol{F}^{\mathrm{e}} \tag{5}$$

where both are related through the following identity, $\boldsymbol{C}^{\mathrm{e}} = \boldsymbol{F}^{\mathrm{g}-\mathrm{t}} \cdot \boldsymbol{C} \cdot \boldsymbol{F}^{\mathrm{g}-1}$. Finally, we introduce the pull back of the spatial velocity gradient $\boldsymbol{l}$ to the intermediate configuration,

$$\boldsymbol{F}^{\mathrm{e}-1} \cdot \boldsymbol{l} \cdot \boldsymbol{F}^{\mathrm{e}} = \boldsymbol{L}^{\mathrm{e}} + \boldsymbol{L}^{\mathrm{g}} \quad \text{with } \boldsymbol{l} = \dot{\boldsymbol{F}} \cdot \boldsymbol{F}^{-1} \tag{6}$$

which obeys the additive split into the elastic velocity gradient $\boldsymbol{L}^{\mathrm{e}} = \boldsymbol{F}^{\mathrm{e}-1} \cdot \dot{\boldsymbol{F}}^{\mathrm{e}}$ and the growth velocity gradient $\boldsymbol{L}^{\mathrm{g}} = \dot{\boldsymbol{F}}^{\mathrm{g}} \cdot \boldsymbol{F}^{\mathrm{g}-1}$. Here, we have applied the notation $\{\dot{\circ}\} = \partial_t\{\circ\}|_{\boldsymbol{X}}$ to denote the material time derivative of any field $\{\circ\}(\boldsymbol{X}, t)$ at fixed material placement $\boldsymbol{X}$.

2.2. Balance equations of area growth

We characterize growing tissue using the framework of open system thermodynamics in which the material density ρ_0 is allowed to change as a consequence of growth (Kuhl and Steinmann, 2003a,b). The balance of mass for open systems balances its rate of change $\dot{\rho}_0$ with a possible in- or outflux of mass $\boldsymbol{R}$ and mass source $\mathcal{R}_0$ (Pang et al., in press;

Taylor et al., 2009):

$$\dot{\rho}_0 = \mathrm{Div}(\boldsymbol{R}) + \mathcal{R}_0 \tag{7}$$

Similarly, the balance of linear momentum balances the density-weighted rate of change of the momentum $\dot{\boldsymbol{v}}$, where $\boldsymbol{v} = \dot{\boldsymbol{\varphi}}$ is nothing but the spatial velocity, with the momentum flux $\boldsymbol{P} = \boldsymbol{F} \cdot \boldsymbol{S}$ and the momentum source $\rho_0 \boldsymbol{b}$.

$$\rho_0 \dot{\boldsymbol{v}} = \mathrm{Div}(\boldsymbol{F} \cdot \boldsymbol{S}) + \rho_0 \boldsymbol{b} \tag{8}$$

Herein, $\boldsymbol{P}$ and $\boldsymbol{S}$ are the first and second Piola–Kirchhoff stress tensors, respectively. Last, we would like to point out that the dissipation inequality of open systems

$$\rho_0 \mathcal{D} = \boldsymbol{S} : \tfrac{1}{2}\dot{\boldsymbol{C}} - \rho_0 \dot{\psi} - \rho_0 \mathcal{S} \geq 0 \tag{9}$$

typically contains an extra entropy source $\rho_0 \mathcal{S}$ to account for the growing nature of living biological systems (Kuhl and Steinmann, 2003a; Menzel, 2005). Eqs. (8) and (9) represent the mass-specific versions of the balance of momentum and of the dissipation inequality which are particularly useful in the context of growth since they contain no explicit dependencies on the changes in mass (Kuhl and Steinmann, 2003b).

2.3. Constitutive equations of area growth

To close the set of equations, we introduce the constitutive equations for the mass flux $\boldsymbol{R}$, for the mass source $\mathcal{R}_0$, for the momentum flux $\boldsymbol{S}$, for the momentum source $\boldsymbol{b}$, and for the growth tensor $\boldsymbol{F}^g$. For the mass flux $\boldsymbol{R}$, we adopt a definition in analogy to Fick's law,

$$\boldsymbol{R} = \boldsymbol{D} \cdot \nabla \rho_0 \tag{10}$$

and relate it directly to the density gradient $\nabla \rho_0$ through the conductivity tensor $\boldsymbol{D}$ (Kuhl et al., 2003). In the case of transversely isotropic in-plane mass conduction, the conductivity tensor $\boldsymbol{D} = d_0[\boldsymbol{I} - \boldsymbol{n}_0 \otimes \boldsymbol{n}_0]$ reduces to the second order tensor for transverse isotropy $[\boldsymbol{I} - \boldsymbol{n}_0 \otimes \boldsymbol{n}_0]$ scaled by the mass conduction coefficient d_0, which has the unit of length squared divided by the time. Immunocytochemistry has shown that expanded tissue undergoes normal epidermal cell differentiation (Wollina et al., 1992). Accordingly, we assume that the newly grown skin has the same density as the initial tissue. This implies that the mass source

$$\mathcal{R}_0 = \rho_0 \,\mathrm{tr}(\boldsymbol{L}^g) \tag{11}$$

can be expressed as the density-weighted trace of the growth velocity gradient $\mathrm{tr}(\boldsymbol{L}^g) = \dot{\boldsymbol{F}}^g : \boldsymbol{F}^{g-t}$ (Himpel et al., 2005). For the sake of transparency, we model skin as an elastic material that can be characterized exclusively in terms of the Helmholtz free energy $\psi = \hat{\psi}(\boldsymbol{C}, \boldsymbol{F}^g)$, which we can use to evaluate the dissipation inequality (9).

$$\rho_0 \mathcal{D} = \left[\boldsymbol{S} - \rho_0 \frac{\partial \psi}{\partial \boldsymbol{C}} \right] : \frac{1}{2}\dot{\boldsymbol{C}} + \boldsymbol{M}^e : \boldsymbol{L}^g - \rho_0 \frac{\partial \psi}{\partial \rho_0} \mathcal{R}_0 - \rho_0 \mathcal{S}_0 \geq 0 \tag{12}$$

Similar to finite strain plasticity (Lee, 1969), we observe that the Mandel stress of the intermediate configuration $\boldsymbol{M}^e = \boldsymbol{C}^e \cdot \boldsymbol{S}^e$ is energetically conjugate to the growth velocity gradient $\boldsymbol{L}^g = \dot{\boldsymbol{F}}^g \cdot \boldsymbol{F}^{g-1}$. From the dissipation inequality (12), we obtain the definition of the second Piola Kirchhoff stress $\boldsymbol{S}$ as thermodynamically conjugate quantity to the right Cauchy Green deformation tensor $\boldsymbol{C}$:

$$\boldsymbol{S} = 2\rho_0 \frac{\partial \psi}{\partial \boldsymbol{C}} = 2\frac{\partial \psi}{\partial \boldsymbol{C}^e} : \frac{\partial \boldsymbol{C}^e}{\partial \boldsymbol{C}} = \boldsymbol{F}^{g-1} \cdot \boldsymbol{S}^e \cdot \boldsymbol{F}^{g-t} \quad \text{with} \ \boldsymbol{S}^e := 2\rho_0 \frac{\partial \psi}{\partial \boldsymbol{C}^e} \tag{13}$$

As a side remark, the elastic constitutive moduli L^e can be obtained by taking the second derivative of the Helmholtz free energy ψ with respect to the elastic part of the deformation gradient $\boldsymbol{F}^e$:

$$\mathsf{L}^e = 2\frac{\partial \boldsymbol{S}^e}{\partial \boldsymbol{C}^e} = 4\rho_0 \frac{\partial^2 \psi}{\partial \boldsymbol{C}^e \otimes \partial \boldsymbol{C}^e} \tag{14}$$

Motivated by clinical observations (Rivera et al., 2005), we represent growth as a strain-driven, transversely isotropic, irreversible process. It is characterized through one single growth multiplier ϑ^g that reflects the irreversible area increase perpendicular to the skin normal $\boldsymbol{n}_0$:

$$\boldsymbol{F}^g = \sqrt{\vartheta^g}\boldsymbol{I} + [1 - \sqrt{\vartheta^g}]\boldsymbol{n}_0 \otimes \boldsymbol{n}_0 \tag{15}$$

For this particular transversely isotropic definition of the growth tensor, for which the material is not allowed to grow in the thickness direction (van der Kolk et al., 1987), the area growth is identical to the volume growth, i.e., $\vartheta^g = \det(\boldsymbol{F}^g) = J^g$. Because of the simple rank-one update structure, we can apply the Sherman–Morrison formula to invert the growth tensor in explicit form:

$$\boldsymbol{F}^{g-1} = \frac{1}{\sqrt{\vartheta^g}}\boldsymbol{I} + \left[1 - \frac{1}{\sqrt{\vartheta^g}}\right]\boldsymbol{n}_0 \otimes \boldsymbol{n}_0 \tag{16}$$

Author's personal copy

2182   *A.B. Tepole et al. / J. Mech. Phys. Solids 59 (2011) 2177–2190*

It introduces the following simple expression for the growth velocity gradient:

$$\boldsymbol{L}^{\mathrm{g}} = \frac{\sqrt{\dot{\vartheta}^{\mathrm{g}}}}{\sqrt{\vartheta^{\mathrm{g}}}}\boldsymbol{I} + \left[1 - \frac{\sqrt{\dot{\vartheta}^{\mathrm{g}}}}{\sqrt{\vartheta^{\mathrm{g}}}}\right]\boldsymbol{n}_0 \otimes \boldsymbol{n}_0 \qquad (17)$$

which proves convenient to explicitly evaluate the mass source as $\mathcal{R}_0 = \rho_0[1 + + 2\sqrt{\dot{\vartheta}}^{\mathrm{g}}/\sqrt{\vartheta^{\mathrm{g}}}]$. Motivated by physiological observations of stretch-induced skin expansion (Gosain et al., 2009), we adopt the following evolution equation for the growth multiplier:

$$\dot{\vartheta}^{\mathrm{g}} = k^{\mathrm{g}}(\vartheta^{\mathrm{g}})\phi^{\mathrm{g}}(\vartheta^{\mathrm{e}}) \qquad (18)$$

which follows a well-established functional form (Lubarda and Hoger, 2002), but is now rephrased in a strain-driven format (Göktepe et al., 2010a, 2010b). To control unbounded growth, we introduce the weighting function

$$k^{\mathrm{g}} = \frac{1}{\tau}\left[\frac{\vartheta^{\mathrm{max}} - \vartheta^{\mathrm{g}}}{\vartheta^{\mathrm{max}} - 1}\right]^{\gamma} \quad \text{with} \quad \frac{\partial k^{\mathrm{g}}}{\partial \vartheta^{\mathrm{g}}} = -\frac{\gamma}{\vartheta^{\mathrm{max}} - \vartheta^{\mathrm{g}}}k^{\mathrm{g}} \qquad (19)$$

where τ denotes the adaptation speed, γ calibrates the shape of the adaptation curve, and $\vartheta^{\mathrm{max}} > 1$ denotes the maximum area growth (Himpel et al., 2005; Lubarda and Hoger, 2002). The growth criterion

$$\phi^{\mathrm{g}} = \vartheta^{\mathrm{e}} - \vartheta^{\mathrm{crit}} = \frac{\vartheta}{\vartheta^{\mathrm{g}}} - \vartheta^{\mathrm{crit}} \quad \text{with} \quad \frac{\partial \phi^{\mathrm{g}}}{\partial \vartheta^{\mathrm{g}}} = -\frac{1}{\vartheta^{\mathrm{g}2}}\vartheta \qquad (20)$$

is driven by the elastic area stretch $\vartheta^{\mathrm{e}} = \vartheta/\vartheta^{\mathrm{g}}$, such that growth is activated only if the elastic area stretch exceeds a critical physiological threshold value $\vartheta^{\mathrm{crit}}$ (Göktepe et al., 2010a). For displacement-driven skin expansion, the model displays a characteristic relaxation-type response, while for force-driven skin expansion, it shows a creep-type behavior (Buganza Tepole et al., submitted for publication).

3. Computational modeling of area growth

The governing equations for finite growth introduced in the previous section are complex and highly nonlinear. In this section, we illustrate their computational solution within an incremental iterative nonlinear finite element framework. To characterize the growth process at each instant in time, we introduce the growth multiplier ϑ^{g} as an internal variable, and solve its evolution equation (18) locally at each integration point using the finite difference method. To explore the interplay between growth and mechanics, we discretize the governing equations for finite growth (2), (8), and (13) in space using the finite element method. In this section, we first derive the discrete local residual and the corresponding tangent moduli for the local Newton iteration to iteratively determine the growth multiplier ϑ^{g}. Then, we derive the stresses $\boldsymbol{S}$ for the discrete global residual and the constitutive moduli $\mathbf{L}$ for the tangent moduli for the global Newton iteration to iteratively determine the deformation $\boldsymbol{\varphi}$.

3.1. Local Newton iteration—growth multiplier

To discretize the biological equilibrium equation (18) in time, we partition the time interval of interest $\mathcal{T}$ into n_{stp} subintervals,

$$\mathcal{T} = \overset{n_{\mathrm{stp}}}{\underset{n=1}{\mathbf{U}}}[t_n, t_{n+1}] \qquad (21)$$

and focus on the interval $[t_n, t_{n+1}]$ for which $\Delta t = t_{n+1} - t_n > 0$ denotes the current time increment. Our goal is to determine the current growth multiplier ϑ^{g} for a given deformation state $\boldsymbol{F}$ at time t, and a given growth multiplier ϑ_n^{g} at the end of the previous time step t_n. For the sake of compactness, here and from now on, we omit the index $(\circ)_{n+1}$ for all quantities at the end of the current time step t_{n+1}. To evaluate the material time derivative of the growth multiplier $\dot{\vartheta}$, we introduce the following approximation:

$$\dot{\vartheta}^{\mathrm{g}} = \frac{1}{\Delta t}[\vartheta^{\mathrm{g}} - \vartheta_n^{\mathrm{g}}] \qquad (22)$$

In the spirit of implicit time stepping schemes, we now reformulate the evolution equation (18) with the help of Eq. (22), introducing the discrete residual R^{ϑ} in terms of the unknown growth multiplier ϑ^{ϑ}:

$$\mathsf{R}^{\vartheta} = \vartheta^{\mathrm{g}} - \vartheta_n^{\mathrm{g}} - k^{\mathrm{g}}\phi^{\mathrm{g}}\Delta t \doteq 0 \qquad (23)$$

We suggest to solve this nonlinear residual equation for the unknown growth multiplier using a local Newton iteration. Within each iteration step, we calculate the linearization of the residual R^{ϑ} with respect to the growth multiplier ϑ^{g},

$$\mathsf{K}^{\vartheta} = \frac{\partial \mathsf{R}^{\vartheta}}{\partial \vartheta^{\mathrm{g}}} = 1 - \left[\frac{\partial k^{\mathrm{g}}}{\partial \vartheta^{\mathrm{g}}}\phi^{\mathrm{g}} + k^{\mathrm{g}}\frac{\partial \phi^{\mathrm{g}}}{\partial \vartheta^{\mathrm{g}}}\right]\Delta t \qquad (24)$$

with the weighting function k^{g} and the growth criterion ϕ^{g} introduced in Eqs. (19) and (20). Within each iteration step, we calculate the iterative update of the unknown growth multiplier $\vartheta^{\mathrm{g}} \leftarrow \vartheta^{\mathrm{g}} - \mathsf{R}^{\vartheta}/\mathsf{K}^{\vartheta}$ until convergence is achieved, i.e., until the local

A.B. Tepole et al. / J. Mech. Phys. Solids 59 (2011) 2177–2190

2183

growth update $\Delta\vartheta^g = -R^\vartheta/K^\vartheta$ is below a user-defined threshold value. In what follows, we will assume that mass diffusion is significantly smaller than the mass source, and therefore negligible, i.e., $\boldsymbol{R} = \boldsymbol{0}$. This implies that, if necessary, the remaining balance of mass, $\dot{\rho}_0 = \rho_0[1 + 2\sqrt{\vartheta}^g/\sqrt{\vartheta^g}]$, can simply be evaluated locally in a post-processing step once local convergence is achieved.

3.2. Global Newton iteration—growing skin

With the simplifying assumptions of a vanishing momentum source, $\boldsymbol{b} = \boldsymbol{0}$, and negligible inertia effects, $\dot{\boldsymbol{v}} = \boldsymbol{0}$, the mechanical equilibrium equation (8) reduces to the internal force balance, $\mathrm{Div}(\boldsymbol{F} \cdot \boldsymbol{S}) \doteq \boldsymbol{0}$. We cast it into its weak form, $\int_{\mathcal{B}_0} \nabla\delta\boldsymbol{\varphi} : [\boldsymbol{F} \cdot \boldsymbol{S}]\, \mathrm{d}V = 0$, through the multiplication with the test function $\delta\boldsymbol{\varphi}$ and the integration over the domain of interest $\mathcal{B}_0$, to solve it globally on the node point level. To discretize it in space, we partition the domain of interest $\mathcal{B}_0$ into n_{el} finite elements $\mathcal{B}_0^e$.

$$\mathcal{B}_0 = \overset{n_{el}}{\underset{e=1}{\mathsf{U}}} \mathcal{B}_0^e \tag{25}$$

Our goal is to determine the deformation state $\boldsymbol{\varphi}$ for a given loading at time t. To approximate the test function $\delta\boldsymbol{\varphi}$, the unknown deformation $\boldsymbol{\varphi}$, and their gradients $\nabla\delta\boldsymbol{\varphi}$ and $\nabla\boldsymbol{\varphi}$, we apply an isoparametric Bubnov–Galerkin based finite element interpolation,

$$\delta\boldsymbol{\varphi} = \sum_{i=1}^{n_{en}} N^i \delta\boldsymbol{\varphi}_i, \quad \nabla\delta\boldsymbol{\varphi} = \sum_{i=1}^{n_{en}} \delta\boldsymbol{\varphi}_i \otimes \nabla N^i, \quad \boldsymbol{\varphi} = \sum_{j=1}^{n_{en}} N^j \boldsymbol{\varphi}_j, \quad \nabla\boldsymbol{\varphi} = \sum_{j=1}^{n_{en}} \boldsymbol{\varphi}_j \otimes \nabla N^j \tag{26}$$

where N^i, N^j are the element shape functions and $i,j = 1,..,n_{en}$ are the element nodes. We now reformulate the weak form of the balance of linear momentum (8) with the help of these finite element approximations, introducing the discrete residual $\mathbf{R}_I^\varphi$ in terms of the unknown nodal deformation $\boldsymbol{\varphi}_J$:

$$\mathbf{R}_I^\varphi = \overset{n_{el}}{\underset{e=1}{\mathsf{A}}} \int_{\mathcal{B}_e} \nabla N_\varphi^i \cdot [\boldsymbol{F} \cdot \boldsymbol{S}]\, \mathrm{d}V_e \doteq \boldsymbol{0} \tag{27}$$

Herein, the operator $\mathbf{A}$ symbolizes the assembly of all element residuals at the $j = 1,..,n_{en}$ element nodes to the global residual at the global node points $J = 1,..,n_{el}$. We can evaluate the global discrete residual (27), once we have iteratively determined the growth multiplier ϑ^g for the given deformation state $\boldsymbol{F}$ and the given history ϑ_n^g as described in Section 3.1. Then we can successively determine the growth tensor $\boldsymbol{F}^g$ from Eq. (15), the elastic tensor $\boldsymbol{F}^e = \boldsymbol{F} \cdot \boldsymbol{F}^{g-1}$ from Eq. (2), the elastic stress $\boldsymbol{S}^e$ from Eq. (13), and lastly, the second Piola Kirchhoff stress $\boldsymbol{S}$:

$$\boldsymbol{S} = 2\frac{\partial\psi}{\partial\boldsymbol{C}} = 2\frac{\partial\psi}{\partial\boldsymbol{C}^e} : \frac{\partial\boldsymbol{C}^e}{\partial\boldsymbol{C}} = \boldsymbol{F}^{g-1} \cdot \boldsymbol{S}^e \cdot \boldsymbol{F}^{g-t} \tag{28}$$

Again, we suggest an incremental iterative Newton algorithm to solve the nonlinear residual equation for the unknown deformation (27). The consistent linearization of the residual $\mathbf{R}_I^\varphi$ with respect to the nodal vector of unknowns $\boldsymbol{\varphi}_J$ introduces the global stiffness matrix:

$$\mathbf{K}_{IJ}^\varphi = \frac{\partial\mathbf{R}_I^\varphi}{\partial\boldsymbol{\varphi}_J} = \overset{n_{el}}{\underset{e=1}{\mathsf{A}}} \int_{\mathcal{B}_e} [\nabla N_\varphi^i \cdot \boldsymbol{F}]^{sym} \cdot \mathbf{L} \cdot [\boldsymbol{F}^t \cdot \nabla N_\varphi^j]^{sym}\, \mathrm{d}V_e + \int_{\mathcal{B}_e} \nabla N_\varphi^i \cdot \boldsymbol{S} \cdot \nabla N_\varphi^j \boldsymbol{I}\, \mathrm{d}V_e \tag{29}$$

The fourth order tensor $\mathbf{L}$ denotes the Lagrangian constitutive moduli which we can determine directly from the linearization of the Piola Kirchhoff stress $\boldsymbol{S}$ with respect to the total right Cauchy Green tensor $\boldsymbol{C}$:

$$\mathbf{L} = 2\frac{\mathrm{d}\boldsymbol{S}}{\mathrm{d}\boldsymbol{C}} = 2\frac{\partial\boldsymbol{S}}{\partial\boldsymbol{C}}\bigg|_{\boldsymbol{F}^g} + 2\left[\frac{\partial\boldsymbol{S}}{\partial\boldsymbol{F}^g} : \frac{\partial\boldsymbol{F}^g}{\partial\vartheta^g}\right] \otimes \frac{\partial\vartheta^g}{\partial\boldsymbol{C}}\bigg|_{\boldsymbol{F}} \tag{30}$$

The first term

$$2\frac{\partial\boldsymbol{S}}{\partial\boldsymbol{C}} = 2\frac{\partial[\boldsymbol{F}^{g-1} \cdot \boldsymbol{S}^e \cdot \boldsymbol{F}^{g-t}]}{\partial\boldsymbol{C}} = [\boldsymbol{F}^{g-1}\overline{\otimes}\boldsymbol{F}^{g-1}] : \mathbf{L}^e : [\boldsymbol{F}^{g-t}\overline{\otimes}\boldsymbol{F}^{g-t}] \tag{31}$$

represents the pull back of the elastic moduli $\mathbf{L}^e$ onto the reference configuration, where $\mathbf{L}^e = 2\partial\boldsymbol{S}^e/\partial\boldsymbol{C}^e$ are the constitutive moduli of the elastic material model as introduced in Eq. (14). The second term

$$\frac{\partial\boldsymbol{S}}{\partial\boldsymbol{F}^g} = \frac{\partial[\boldsymbol{F}^{g-1} \cdot \boldsymbol{S}^e \cdot \boldsymbol{F}^{g-t}]}{\partial\boldsymbol{F}^g} = -[\boldsymbol{F}^{g-1}\overline{\otimes}\boldsymbol{S} + \boldsymbol{S}\underline{\otimes}\boldsymbol{F}^{g-1}] - [\boldsymbol{F}^{g-1}\overline{\otimes}\boldsymbol{F}^{g-1}] : \frac{1}{2}\mathbf{L}^e : [\boldsymbol{F}^{g-t}\underline{\otimes}\boldsymbol{C}^e + \boldsymbol{C}^e\overline{\otimes}\boldsymbol{F}^{g-t}] \tag{32}$$

consists of two contributions that resemble a geometric and a material stiffness contribution known from nonlinear continuum mechanics. The third term

$$\frac{\partial\boldsymbol{F}^g}{\partial\vartheta^g} = \frac{1}{2\sqrt{\vartheta^g}}[\boldsymbol{I} - \boldsymbol{n}_0 \otimes \boldsymbol{n}_0] \tag{33}$$

and the fourth term

$$\frac{\partial \vartheta^g}{\partial \boldsymbol{C}} = \left[\frac{1}{\tau}\frac{1}{\vartheta^g}\left[\frac{\vartheta^{max}-\vartheta^g}{\vartheta^{max}-1}\right]^{\gamma}\frac{1}{K^g}\Delta t\right]\left[\frac{1}{2}\vartheta\boldsymbol{C}^{-1}-\frac{1}{2}\frac{J^2}{\vartheta}[\boldsymbol{C}^{-1}\cdot\boldsymbol{n}_0]\otimes[\boldsymbol{C}^{-1}\cdot\boldsymbol{n}_0]\right] \tag{34}$$

depend on the particular choice for the growth tensor $\boldsymbol{F}^g$ in Eq. (15) and on the evolution equation for the growth multiplier ϑ^g in Eq. (18), respectively. For each global Newton iteration step, we iteratively update the current deformation state $\boldsymbol{\varphi}\leftarrow\boldsymbol{\varphi}-\boldsymbol{K}_{IJ}^{\varphi-1}\cdot\boldsymbol{R}_I^{\varphi}$ until we achieve algorithmic convergence. Upon convergence, we store the corresponding growth multipliers ϑ^g at the integration point level. To solve these nonlinear finite element equations, we implement the growth model in a custom-designed version of the multipurpose nonlinear finite element program FEAP (Taylor, 2008).

4. Example of skin expansion and growth

In this section, we specify the constitutive equations, the material parameters, the geometry, and the finite element discretization to model skin growth induced through tissue expansion. We focus on two different load cases, tissue expander inflation to simulate skin growth, and tissue expander deflation to simulate residual stresses.

4.1. Model problem of tissue expander inflation and deflation

To focus on the impact of growth, we assume a generic isotropic Neo-Hookean baseline elasticity and specify the free energy in the following form:

$$\rho_0\psi = \tfrac{1}{2}\lambda\ln^2(J^e)+\tfrac{1}{2}\mu[\boldsymbol{C}^e:\boldsymbol{I}-3-2\ln(J^e)]$$

According to Eqs. (13) and (14), we can then express the elastic second Piola Kirchhoff stress $\boldsymbol{S}^e=2\partial\psi/\partial\boldsymbol{C}^e$ as

$$\boldsymbol{S}^e = [\lambda\ln(J^e)-\mu]\boldsymbol{C}^{e-1}+\mu\boldsymbol{I}$$

and the elastic constitutive moduli $\boldsymbol{L}^e=2\partial\boldsymbol{S}^e/\partial\boldsymbol{C}^e$ as

$$\boldsymbol{L}^e = \lambda\boldsymbol{C}^{e-1}\otimes\boldsymbol{C}^{e-1}+[\mu-\lambda\ln(J^e)][\boldsymbol{C}^e\overline{\otimes}\boldsymbol{C}^e+\boldsymbol{C}^e\underline{\otimes}\boldsymbol{C}^e]$$

Here we have used the common abbreviations, $\{\bullet\overline{\otimes}\circ\}_{ijkl}=\{\bullet\}_{ik}\{\circ\}_{jl}$ and $\{\bullet\underline{\otimes}\circ\}_{ijkl}=\{\bullet\}_{il}\{\circ\}_{jk}$, for the non-standard fourth order products. For the elastic model, we assume Lamé constants of $\lambda=0.577$ and $\mu=0.0385$ and an initial density of $\rho_0^{init}=1.0$ (Himpel et al., 2005). For the growth model, we assume that growth takes place above the critical threshold of $\vartheta^{crit}=1.01$, we restrict the maximum area growth to $\vartheta^{max}=2.4$, we assume an adaptation speed of $\tau=1.0$, and a growth exponent of $\gamma=2.0$. Sensitivity analyses demonstrate that the material parameters τ and γ influence the adaptation time and the shape of the adaptation curve (Himpel et al., 2005), but not the final state of biological equilibrium (Rausch et al., in press; Schmid et al., in press). We model the skin area under consideration as a 0.2 cm thin 12×12 cm^2 square sheet, discretized with $3\times24\times24=1728$ trilinear brick elements, with $4\times25\times25=2500$ nodes and 7500 degrees of freedom. To explore the impact of different tissue expander geometries, we model a circular, a square, a rectangular, and a crescent-shaped expander. For the sake of comparison, the base surface area of all four expanders is scaled to a size of $A_0=37$ cm^2. As illustrated in Fig. 4, we can then model tissue expansion by pressuring the corresponding 148 light red elements from underneath while fixing the bottom nodes of all remaining white elements.

The pressure is increased linearly in 40 steps of $\Delta t=0.1$ to a maximum pressure of $p=0.002$ at $t=4$. We then keep the pressure constant and watch the skin grow. In Section 4.2, we explore skin growth upon tissue expander inflation. To allow the skin to gradually grow towards its biological equilibrium state, we keep the pressure constant for another 460 steps until $t=50$. In Section 4.3, we explore the growth-induced residual stresses upon tissue expander deflation. We keep the pressure constant for another 80 steps until $t=12$, and then gradually decrease the pressure back to zero throughout another 30 time steps until $t=15$.
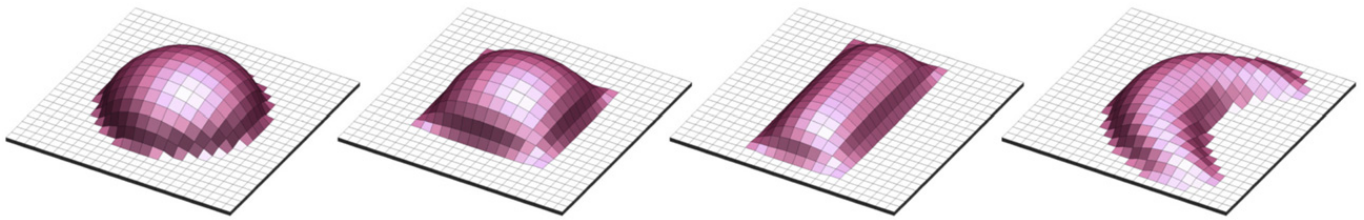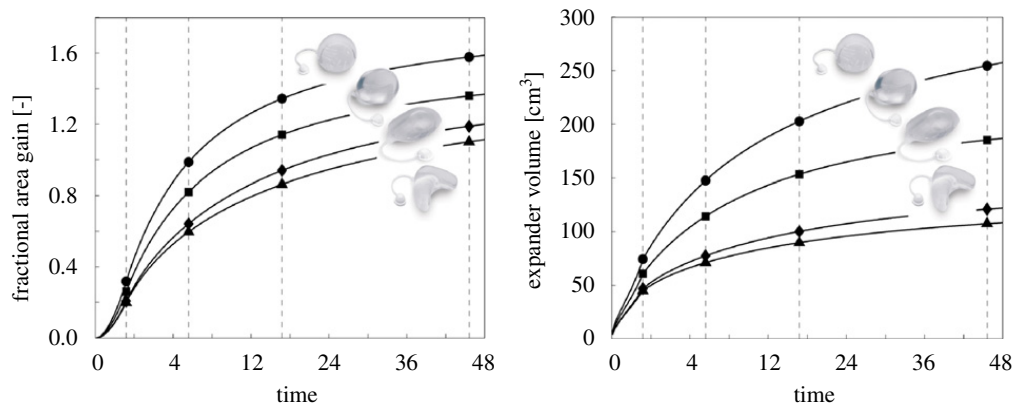

Fig. 4. Tissue expander inflation and deflation. Skin is modeled as a 0.2 cm thin 12×12 cm^2 square sheet, discretized with $3\times24\times24=1728$ trilinear brick elements, with $4\times25\times25=2500$ nodes and 7500 degrees of freedom. We explore the impact of different tissue expander geometries, circular, square, rectangular, and crescent-shaped. The base surface area of all expanders is scaled to 148 elements corresponding to 37 cm^2. This area, here shown in light red, is gradually pressurized from underneath while the bottom nodes of all remaining elements, shown in white, are fixed. (For interpretation of the references to color in this figure legend, the reader is referred to the web version of this article.)

4.2. Tissue expander inflation—skin growth

Fig. 5 displays the fractional area gain and the increasing expander volume in response to tissue expander inflation. We model expander inflation through gradually increasing the pressure from time $t=0$ to 4, and then hold it constant from time $t=4$ to 50. Under the same pressure, we observe that the circular expander triggers the largest fractional area gain, followed by the square, the rectangular, and the crescent-shaped expanders, Fig. 5, left. Since the base surface area is the same for all four expanders, this implies that the expander volume is largest for the circular expander, followed by the square, the rectangular, and the crescent-shaped expanders, Fig. 5, right. Both graphs demonstrate the characteristic creep-type growth under constant pressure with a gradual convergence towards the biological equilibrium state.

Table 1 displays a quantitative comparison of the four different tissue expander geometries. Following a linearly increasing and then constant pressure, at $t=50$, the maximum growth multiplier is largest for the circular expander, with $\vartheta^g = 2.364$, followed by $\vartheta^g = 2.349$ for the square expander, $\vartheta^g = 2.257$ for the rectangular expander, and $\vartheta^g = 2.247$ for the crescent-shaped expander. While the maximum area growth ϑ^g is nothing but a local measure of growth, the global absolute area gain ΔA characterizes the total amount of skin growth. Skin growth is again largest for the circular expander with $\Delta A = 58.738$ cm^2, followed by the square expander with 50.627 cm^2, the rectangular expander with 44.398 cm^2, and the crescent-shaped expander with 41.186 cm^2, meaning that the total area of $A_0 = 37$ cm^2 has more than doubled in all four cases. This implies that the fractional area gain ranges from 1.588 for the circular expander to 1.368, 1.200, and 1.113 for the square, the rectangular, and the crescent-shaped expanders, Fig. 5, left. To obtain these area gains, the required expander volumes are 257.451 cm^3 for the circular expander, 186.771 cm^3 for the square expander, 122.063 cm^3 for the rectangular expander, and 108.416 cm^3 for the crescent-shaped expander. These values agree nicely with the rectangular expander volumes of 100–200 cm^3 typically used in the forehead and are slightly lower than the expander volumes of 140–600 cm^3 used in the scalp during pediatric forehead reconstruction (Gosain et al., 2009).

Fig. 6 summarizes the spatio-temporal evolution of area growth for all four expander types. Snapshots correspond to $t=4$, 12, 24, and 48, from left to right, corresponding to the labels and dashed vertical lines in Fig. 5. The color code illustrates the evolution of the growth multiplier ϑ^g ranging from $\vartheta^g = 1.0$ for the initially ungrown skin, shown in blue, to $\vartheta^g = \vartheta^{max} = 2.4$ for the fully grown state, shown in red. Fig. 6 confirms that the circular expander induces the largest amount of growth followed by the square, the rectangular, and the crescent-shaped expanders. Remarkably, despite the
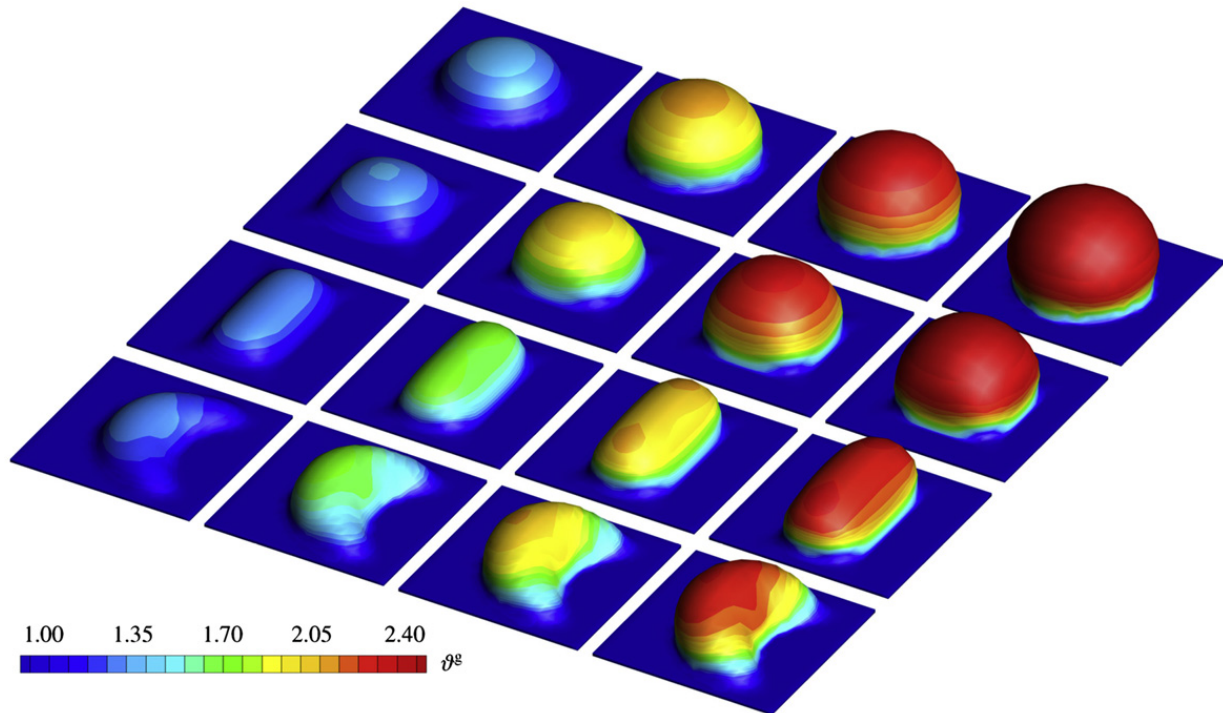

Fig. 5. Tissue expander inflation. Temporal evolution of fractional area gain and increasing expander volume. Expanders are inflated gradually between $t=0$ and 4 by linearly increasing the pressure. The pressure is then held constant from $t=4$ to 50 to allow the skin to grow. Under the same pressure applied to the same base surface area, the circular expander displays the largest fractional area gain, followed by the square, the rectangular, and the crescent-shaped expanders, left. Growth causes the tissue to relax and the expander volume to increase. The expander volume is largest for the circular expander, followed by the square, the rectangular, and the crescent-shaped expanders, right. Both graphs demonstrate the characteristic creep-type growth under constant pressure with a gradual convergence towards the biological equilibrium state.

Table 1
Tissue expander inflation and deflation. Maximum growth multiplier, absolute area gain, fractional area gain, and expander volume under constant pressure loading at time $t=50$ are largest for the circular expander, followed by the square, the rectangular, and the crescent shape expanders. Maximum principal residual stresses upon unloading after a constant pressure growth until $t=12$ are largest for the circular expander, followed by the square, the rectangular, and the crescent-shaped expanders.

	Maximum growth ϑ^g (−)	Initial area A_0 (cm^2)	absolute area gain ΔA (cm^2)	Fractional area gain $\Delta A/A_0$ (−)	Expander volume V (cm^3)	Expander pressure p/E (−)	Maximum residual stress σ^{max}/E (−)
Circular	2.364	37.000	58.738	1.588	257.451	0.002	0.419
square	2.349	37.000	50.627	1.368	186.771	0.002	0.410
Rectangular	2.257	37.000	44.398	1.200	122.063	0.002	0.335
Crescent	2.247	37.000	41.186	1.113	108.416	0.002	0.328

Fig. 6. Tissue expander inflation. Spatio-temporal evolution of growth area stretch ϑ^g for circular, square, rectangular, and crescent-shaped expanders. Under the same pressure applied to the same base surface area, the circular expander induces the largest amount of growth followed by the square, the rectangular, and the crescent-shaped expanders. The color code illustrates the evolution of the growth multiplier ϑ^g, ranging from $\vartheta^g = 1.0$ for the initially ungrown skin, shown in blue, to $\vartheta^g = \vartheta^{max} = 2.4$ for the fully grown state, shown in red. Snapshots correspond to $t=4$, 12, 24, and 48, from left to right, corresponding to the labels in Fig. 5. (For interpretation of the references to color in this figure legend, the reader is referred to the web version of this article.)
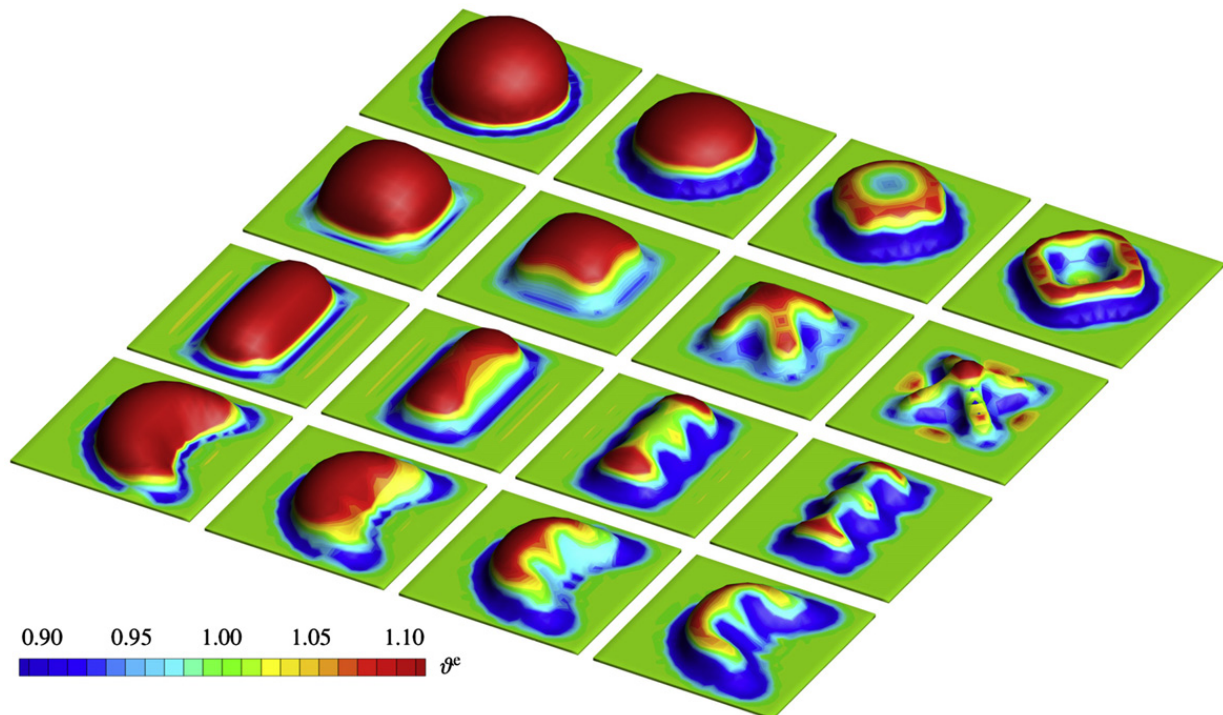
Fig. 7. Tissue expander deflation. Spatio-temporal evolution of elastic area stretch ϑ^e for circular, square, rectangular, and crescent-shaped expanders. As the expander pressure is gradually removed, from left to right, the grown skin layer collapses. Deviations from a flat surface after total unloading, right, demonstrate the irreversibility of the growth process. Growth induces compression at the edges of the original base surface area, and tension in the center region. The color code illustrates the evolution of the elastic area stretch ϑ^e, ranging from $\vartheta^e = 0.9$ corresponding to 10% of area compression, shown in blue, to $\vartheta^e = 1.1$ corresponding to 10% of area tension, shown in red. Snapshots correspond to $t=12$, 13, 14, and 15, from left to right. (For interpretation of the references to color in this figure legend, the reader is referred to the web version of this article.)

large deformations of the thin skin layer, the algorithm always converges quadratically and displays no instabilities, maintaining robustness throughout the entire simulation.

4.3. Tissue expander deflation—residual stress

Fig. 7 documents the spatio-temporal evolution of the elastic area stretch in response to tissue expander deflation. We model expander deflation after gradual inflation from time $t=0$ to 4 and a constant expander pressure from time $t=4$ to 12 through a gradual decrease of the expander pressure back to zero at time $t=15$. Snapshots correspond to $t=12$, 13, 14, and 15, from left to right. Fig. 7 confirms the irreversible nature of skin growth. As the expander pressure is gradually removed, from left to right, the grown skin layer collapses. Deviations from a flat surface after total unloading, right, confirm the irreversibility of the growth process. The color code illustrates the evolution of the elastic area stretch ϑ^e, ranging from $\vartheta^e = 0.9$ corresponding to 10% of area compression, shown in blue, to $\vartheta^e = 1.1$ corresponding to 10% of area tension, shown in red. Growth induces compressive strains at the edges of the original base surface area, and tensile strains in the center region.

Fig. 8 documents the spatio-temporal evolution of the maximum principal stress in response to tissue expander deflation. The four sets of snapshots at $t=12$, 13, 14, and 15 correspond to the same time points shown in the elastic area strain plot of Fig. 7. The color code corresponds to the maximum principal stress σ^{max}, ranging from $\sigma^{max} = 0.0$, shown in blue, to $\sigma^{max} = 0.40$, shown in red. The remaining stresses in the unloaded state, shown in red on the right, correspond to growth-induced residual stresses. While the existence of residual stresses in growing biological tissues has been intensely discussed in the literature (Rodriguez et al., 1994; Taber and Humphrey, 2001; Vandiver and Goriely, 2009), this is one of the first attempts to visually illustrate their existence upon complete unloading. Although the algorithm is capable of robustly simulating total pressure removal after time step $t=12$, we would like to point out that the algorithm struggled to fully unload the biological equilibrium state after $t=50$ discussed in Section 4.2. However, the observed loss of algorithmic convergence upon unloading a severely grown skin sheet is mainly a problem of skin collapse and self-contact rather than that of the conceptual nature of our model.

Finally, to quantify the residual stresses in the unloaded sheet, the last column in Table 1 compares the maximum principal residual stresses for all four expander geometries. In agreement with the other results of this study, residual stresses are largest when using a circular expander with $\sigma^{max} = 0.419$, followed by the square expander with $\sigma^{max} = 0.410$, the rectangular expander with $\sigma^{max} = 0.335$, and the crescent-shaped expander with $\sigma^{max} = 0.328$.
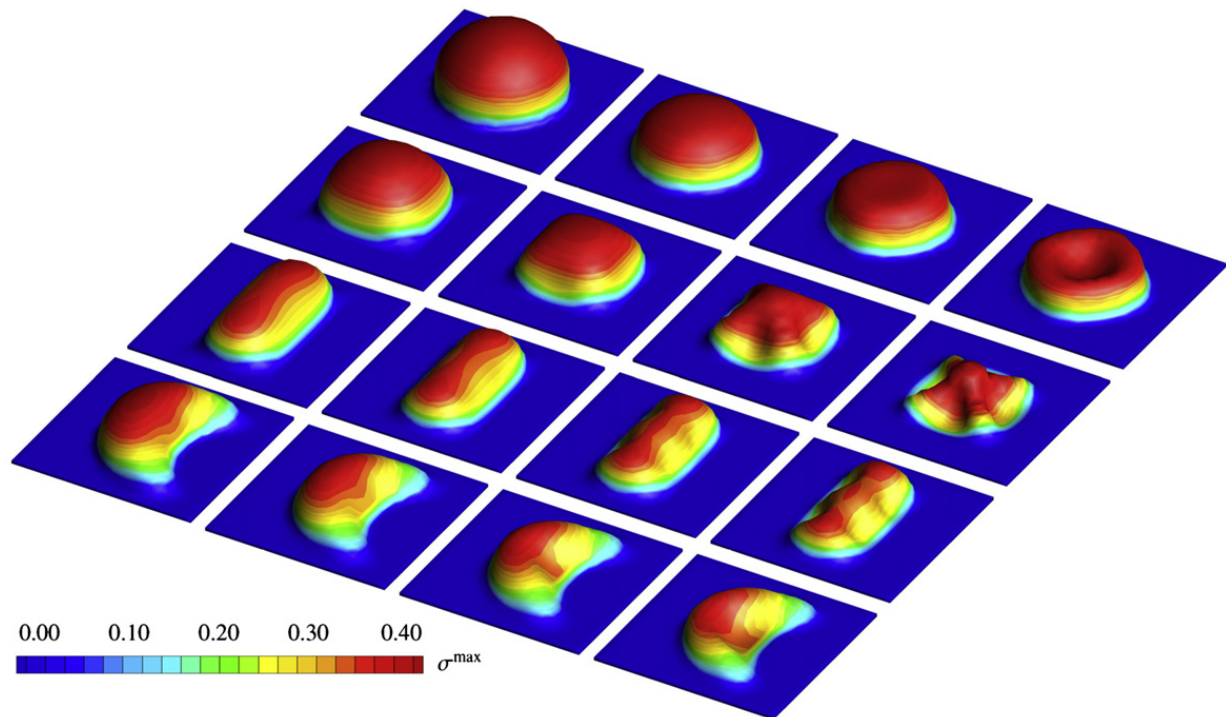
Fig. 8. Tissue expander deflation. Spatio-temporal evolution of maximum principal stress σ^{max} for circular, square, rectangular, and crescent-shaped expanders. As the expander pressure is gradually removed, from left to right, the grown skin layer collapses. Deviations from a flat surface after total unloading, right, demonstrate the irreversibility of the growth process. Remaining stresses at the unloaded state, right, are growth-induced residual stresses. The color code illustrates the evolution of the maximum principal stress σ^{max}, ranging from $\sigma^{max} = 0.0$, shown in blue, to $\sigma^{max} = 0.40$, shown in red. Snapshots correspond to $t=12$, 13, 14, and 15, from left to right. (For interpretation of the references to color in this figure legend, the reader is referred to the web version of this article.)

4.4. Limitations

Although our results hold promise to reliably predict skin growth in response to tissue expansion, we would like to point out that this is only a preliminary study with several limitations. First, we model skin using an isotropic Neo-Hookean baseline elasticity model as specified in Section 4.1. However, adopting a more physiological anisotropic skin model that accounts for pronounced collagen fiber orientations parallel and perpendicular to Langer's lines (Bischoff et al., 2000; Kuhl et al., 2005, 2006) is conceptually straightforward and part of our current research efforts (Buganza Tepole et al., submitted for publication). Along the same lines, it would be slightly more cumbersome, but possible, to introduce a progressive reorientation of the collagen network in response to expansion-induced stretch (Himpel et al., 2008; Kuhl and Holzapfel, 2007; Menzel, 2007). Second, the growth process itself may in fact be anisotropic. Given the modularity of our model, the incorporation of different growth multipliers to characterize growth parallel and perpendicular to Langer's lines would require only minor adjustments (Göktepe et al., 2010b). In particular, it would affect the definition of the growth tensor (15), its inverse (16), and its derivative (33). Third, here, we model the epidermis and the dermis as a single homogenous material, neglecting possible internal stresses caused by the different material properties of these two layers. It would be desirable, in the future, to model both layers individually, to explore the mechanobiology of the epidermal–dermal interface and its functional role in internal–external load transfer (Silver et al., 2003). Especially when discretizing the individual skin layers, it might become essential to model skin using membrane or shell elements to increase computational efficiency, to ensure well-conditioning of the overall system matrix, and to avoid the typical locking effects associated with thin geometries subjected to bending (Socci et al., 2007). Fourth, the calibration of the material parameters for both the elastic model and the growth model remains a question to be addressed in the future (Mazza et al., 2005). Here, for conceptual comparison, we have only used generic material parameter values. As a first step, we have recently refined the constitutive model for skin (Buganza Tepole et al., submitted for publication), and calibrated its parameters using experiments reported in the literature (Kvistedal and Nielsen, 2009; Lanir and Fung, 1974). Fifth, for the sake of simplicity, we model the tissue expander only indirectly through controlling the applied pressure. In real tissue expansion, the control parameter following selection and implantation of the tissue expander is the volume of the expander. This implies that our virtual tissue expansion resembles a creep test under constant loading, while clinical tissue expansion resembles a relaxation test under constant deformation. Last, a more realistic model should incorporate the real expander to account for effects like interface sliding or shear (Socci et al., 2007), and, ideally, also an idealized face (Mazza et al., 2007). In addition, the expander base which we have here modeled as fixed and undeformable, should ideally be modeled as soft bedding. In reality, the expander base presses into the surrounding tissue. Despite tissue expander designs using a semi-rigid base, stretching of the base still occurs and has clinical consequence. When placed on the craniofacial skeleton, temporary but reversible bone deformations have been observed in pediatric patients (LoGiudice and Gosain, 2003). To address these limitations, we are in the process of refining the elastic model, the growth model, and the boundary conditions, to render our future simulations more realistic.

5. Conclusion

In this study, for the first time, we present a fully three-dimensional computational model for tissue expansion and skin growth in reconstructive surgery. Tissue expansion is a common surgical procedure that enables the body to grow extra skin for the resurfacing of large congenital defects of the skin including giant nevi and vascular anomalies and the correction of skin deformity following burn injuries and other forms of traumatic skin loss. Tissue expansion is also widely used for breast reconstruction following the removal of breast cancer. In tissue expansion, a subcutaneous inflatable silicone expander is implanted and gradually filled with saline solution causing the skin to stretch. Increased tissue tension triggers new cells to form and the skin to grow. Skin growth is permanent but will retract to some degree when the expander is removed. Despite intense research in clinical and experimental skin growth, our understanding of the mechano-biological phenomena during tissue expansion remains poor and largely qualitative.

In this paper, we propose to model tissue expansion within the concept of finite growth based on the multiplicative decomposition of the deformation gradient into an elastic and a growth part. We assume that growth is an irreversible, transversely isotropic process which takes place exclusively in the skin layer, while the skin thickness is assumed to remain virtually unaffected. Accordingly, we introduce a single scalar variable, the growth multiplier, to characterize the amount of area growth. To quantify its evolution in time, we suggest a stretch driven growth law which activates growth once the strains exceed a critical physiological threshold level. This model is a significant advancement over existing purely kinematic models in that expander-induced strains are not exclusively attributed to growth alone, but are a result of both growth and elastic deformation. Accordingly, this model potentially avoids the inherent overestimation of net area surface gain observed in existing purely kinematic models.

Since skin growth is a highly nonlinear, heterogeneous process, we propose to solve the governing equations using a nonlinear finite element approach. For the first time, we model area growth in the form of a scalar-valued growth multiplier which we introduce as an internal variable on the integration point level. We evaluate its temporal evolution locally using a finite difference approach. To guarantee maximum efficiency, stability, and optimal convergence of the algorithm, we suggest a local Newton iteration to update the growth multiplier at each integration point, embedded within a global Newton iteration to update the deformation at each finite element node. This approach requires a

A.B. Tepole et al. / J. Mech. Phys. Solids 59 (2011) 2177–2190

2189

consistent linearization of the biological equilibrium equation on the integration point level combined with a consistent linearization of the mechanical equilibrium equation on the node point level. In contrast to existing axisymmetric models, this novel fully 3D approach allows us to model and compare arbitrarily shaped tissue expander geometries.

To explore the features of our model, we simulate skin growth in response to four commonly available tissue expander geometries, circular, square, rectangular, and crescent-shaped. For each geometry, we gradually increase the expander pressure and then hold it constant to allow the skin to grow over time. We explore two scenarios, tissue expander inflation to study skin growth, and tissue expander deflation to study residual stresses. In the first case, we allow progressive skin growth until we reach the biological equilibrium state. For this state, we compare the maximum growth multiplier as a local metric for growth with the fractional area gain as a global metric for growth, and quantify the corresponding expander volumes. We observe that for the same pressure applied to the same base surface area, the circular expander induces the largest amount of growth followed by the square, the rectangular, and the crescent-shaped expanders. In the second case, we gradually remove the expander pressure. For the fully unloaded state, we compare the collapsed tissue shapes in terms of tensile and compressive regions and in terms of residual stresses. This aspect of the work is novel in the sense that the existence of residual stresses has been discussed in the literature, but rarely have they been computationally visualized.

To our knowledge, this is the first study in which skin growth in response to tissue expansion has been addressed from a mechanistic point of view. A comprehensive understanding of the gradually evolving stress and strain fields in growing skin may help the surgeon to optimize clinical process parameters such as expander geometry, expander size, expander placement, and inflation timing. Ultimately, through inverse modeling, computational tools like ours have the potential to rationalize these parameters to obtain skin flaps of desired size and shape. Overall, we believe that predictive computational modeling might open new avenues in reconstructive surgery and enhance treatment for patients with birth defects, burn injuries, or breast tumor removal.

Acknowledgments

References

Ambrosi, D., Mollica, F., 2002. On the mechanics of a growing tumor. Int. J. Eng. Sci. 40, 1297–1316.

Ambrosi, D., Ateshian, G.A., Arruda, E.M., Cowin, S.C., Dumais, J., Goriely, A., Holzapfel, G.A., Humphrey, J.D., Kemkemer, R., Kuhl, E., Olberding, J.E., Taber, L.A., Garikipati, K., 2011. Perspectives on biological growth and remodeling. J. Mech. Phys. Solids 59, 863–883.

Argenta, L.C., Watanabe, M.J., Grabb, W.C., 1983. The use of tissue expansion in head and neck reconstruction. Ann. Plast. Surg. 11, 31–37.

Arneja, J.S., Gosain, A.K., 2005. Giant congenital melanocytic nevi of the trunk and an algorithm for treatment. J. Craniofac. Surg. 16, 886–893.

Arneja, J.S., Gosain, A.K., 2007. Giant congenital melanocytic nevi. Plast. Reconstr. Surg. 120, 26e–40e.

Arneja, J.S., Gosain, A.K., 2009. Giant congenital melanocytic nevi. Plast. Reconstr. Surg. 124, 1e–13e.

Ben Amar, M., Goriely, A., 2005. Growth and instability in elastic tissues. J. Mech. Phys. Solids 53, 2284–2319.

Bischoff, J.E., Arruda, E.M., Grosh, K., 2000. Finite element modeling of human skin using an isotropic, nonlinear elastic constitutive model. J. Biomech. 33, 645–652.

Brobmann, G.F., Huber, J., 1985. Effects of different-shaped tissue expanders on transluminal pressure, oxygen tension, histopathologic changes, and skin expansion in pigs. Plast. Reconstr. Surg. 76, 731–736.

Buganza Tepole, A., Gosain, A.K., Kuhl, E. Stretching skin: the physiological limit and beyond. submitted for publication.

Das, D., Gosain, A.K., 2009. Burned facial skin. In: Hom, D.B., Hebda, P.A., Gosain, A.K., Friedman, C.D. (Eds.), Essential Tissue Healing of the Face and Neck. B.C. Decker, Inc., Hamilton, pp. 181–194.

De Filippo, R.E., Atala, A., 2002. Stretch and growth: the molecular and physiologic influences of tissue expansion. Plast. Reconstr. Surg. 109, 2450–2462.

Dervaux, J., Ben Amar, M., 2011. Buckling consideration in constrained growth. J. Mech. Phys. Solids 59, 538–560.

Dervaux, J., Ciarletta, P., Ben Amar, M., 2009. Morphogenesis of thin hyperelastic plates: a constitutive theory of biological growth in the Föppl–von Karman limit. J. Mech. Phys. Solids 57, 458–471.

Duits, E.H.A., Molenaar, J., van Rappard, J.H.A., 1989. The modeling of skin expanders. Plast. Reconstr. Surg. 83, 362–367.

Dunlop, J.W.C., Fischer, F.D., Gamsjäger, E., Fratzl, P., 2010. A theoretical model for tissue growth in confined geometries. J. Mech. Phys. Solids 58, 1073–1087.

Epstein, M., Maugin, G.A., 2000. Thermomechanics of volumetric growth in uniform bodies. Int. J. Plast. 16, 951–978.

Ganghoffer, J.F., 2010. Mechanical modeling of growth considering domain variation. Part II: volumetric and surface growth involving Eshelby tensors. J. Mech. Phys. Solids 58, 1434–1459.

Garikipati, K., Arruda, E.M., Grosh, K., Narayanan, H., Calve, S., 2004. A continuum treatment of growth in biological tissue: the coupling of mass transport and mechanics. J. Mech. Phys. Solids, 1595–1625.

Garikipati, K., 2009. The kinematics of biological growth. Appl. Mech. Rev. 62, 030801.1–030801.7.

Göktepe, S., Abilez, O.J., Parker, K.K., Kuhl, E., 2010a. A multiscale model for eccentric and concentric cardiac growth through sarcomerogenesis. J. Theor. Biol. 265, 433–442.

Göktepe, S., Abilez, O.J., Kuhl, E., 2010b. A generic approach towards finite growth with examples of athlete's heart, cardiac dilation, and cardiac wall thickening. J. Mech. Phys. Solids 58, 1661–1680.

Goriely, A., BenAmar, M., 2005. Differential growth and instability in elastic shells. Phys. Rev. Lett. 94, 198103.

Goriely, A., Ben Amar, M., 2007. On the definition and modeling of incremental, cumulative, and continuous growth laws in morphoelasticity. Biomech. Model. Mechanobiol. 6, 289–296.

Gosain, A.K., Santoro, T.D., Larson, D.L., Gingrass, R.P., 2001. Giant congenital nevi: a 20-year experience and an algorithm for their management. Plast. Reconstr. Surg. 108, 622–636.

Gosain, A.K., Zochowski, C.G., Cortes, W., 2009. Refinements of tissue expansion for pediatric forehead reconstruction: a 13-year experience. Plast. Reconstr. Surg. 124, 1559–1570.

Himpel, G., Kuhl, E., Menzel, A., Steinmann, P., 2005. Computational modeling of isotropic multiplicative growth. Comput. Model. Eng. Sci. 8, 119–134.

Himpel, G., Menzel, A., Kuhl, E., Steinmann, P., 2008. Time-dependent fibre reorientation of transversely isotropic continua—finite element formulation and consistent linearization. Int. J. Numer. Meth. Eng. 73, 1413–1433.

Humphrey, J., 2002. Cardiovascular Tissue Mechanics: Cells, Tissues, and Organs. Springer.

Kroon, W., Delhaas, T., Arts, T., Bovendeerd, P., 2009. Computational modeling of volumetric soft tissue growth: application to the cardiac left ventricle. Biomech. Model. Mechanobiol. 8, 309–310.

Kuhl, E., Steinmann, P., 2003a. Mass- and volume specific views on thermodynamics for open systems. Proc. R. Soc. 459, 2547–2568.

Kuhl, E., Steinmann, P., 2003b. On spatial and material settings of thermohyperelastodynamics for open systems. Acta Mech. 160, 179–217.

Kuhl, E., Menzel, A., Steinmann, P., 2003. Computational modeling of growth—a critical review, a classification of concepts and two new consistent approaches. Comput. Mech. 32, 71–88.

Kuhl, E., Garikipati, K., Arruda, E.M., Grosh, K., 2005. Remodeling of biological tissue: mechanically induced reorientation of a transversely isotropic chain network. J. Mech. Phys. Solids 53, 1552–1573.

Kuhl, E., Menzel, A., Garikipati, K., 2006. On the convexity of transversely isotropic chain network models. Philos. Mag. 86, 3241–3258.

Kuhl, E., Maas, R., Himpel, G., Menzel, A., 2007. Computational modeling of arterial wall growth: attempts towards patient-specific simulations based on computer tomography. Biomech. Model. Mechanobiol. 6, 321–331.

Kuhl, E., Holzapfel, G.A., 2007. A continuum model for remodeling in living structures. J. Mater. Sci. 2, 8811–8823.

Kvistedal, Y.A., Nielsen, P.M.F., 2009. Estimating material parameters of human skin in vivo. Biomech. Model. Mechanobiol. 8, 1–8.

Lanir, Y., Fung, Y.C., 1974. Two-dimensional mechanical properties of rabbit skin. II. Experimental results. J. Biomech. 7, 171–182.

Lee, E.H., 1969. Elastic–plastic deformation at finite strains. J. Appl. Mech. 36, 1–6.

Li, B., Cao, Y.P., Feng, X.Q., Gao, H., 2011. Surface wrinkling of mucosa induced by volumetric growth: theory, simulation and experiment. J. Mech. Phys. Solids 59, 758–774.

LoGiudice, J., Gosain, A.K., 2003. Pediatric tissue expansion: indications and complications. J. Craniofac. Surg. 14, 866–872.

Lubarda, A., Hoger, A., 2002. On the mechanics of solids with a growing mass. Int. J. Solids Struct. 39, 4627–4664.

Mazza, E., Papes, O., Rubin, M.B., Bodner, S.R., Binur, N.S., 2005. Nonlinear elastic–viscoplastic constitutive equations for aging facial tissues. Biomech. Model. Mechanobiol. 4, 178–189.

Mazza, E., Papes, O., Rubin, M.B., Bodner, S.R., Binur, N.S., 2007. Simulation of the aging face. J. Biomech. Eng. 129, 619–623.

McMahon, J., Goriely, A., 2010. Spontaneous cavitation in growing elastic membranes. Math. Mech. Solids 15, 57–77.

Menzel, A., 2005. Modelling of anisotropic growth in biological tissues—a new approach and computational aspects. Biomech. Model. Mechanobiol. 3, 147–171.

Menzel, A., 2007. A fibre reorientation model for orthotropic multiplicative growth. Biomech. Model. Mechanobiol. 6, 303–320.

Moulton, D.E., Goriely, A., 2011. Circumferential buckling instability of a growing cylindrical tube. J. Mech. Phys. Solids 59, 525–537.

Neumann, C.G., 1959. The expansion of an area of skin by progressive distension of a subcutaneous balloon; use of the method for securing skin for subtotal reconstruction of the ear. Plast. Reconstr. Surg. 19, 124–130.

Pang, H., Shiwalkar, A.P., Madormo, C.M., Taylor, R.E., Andriacchi, T.P., Kuhl, E. Computational modeling of bone density profiles in response to gait: a subject-specific approach. Biomech. Model. Mechanobiol., in press. doi:10.1007/s10237-011-0318-y.

Radovan, C., 1982. Breast reconstruction after mastectomy using the temporary expander. Plast. Reconstr. Surg. 69, 195–208.

Rausch, M.K., Dam, A., Göktepe, S., Abilez, O.J., Kuhl, E. Computational modeling of growth: systemic and pulmonary hypertension in the heart. Biomech. Model. Mechanobiol., in press. doi: 10.1007/s10237-010-0275-x.

Rivera, R., LoGiudice, J., Gosain, A.K., 2005. Tissue expansion in pediatric patients. Clin. Plast. Surg. 32, 35–44.

Rodriguez, E.K., Hoger, A., McCulloch, A.D., 1994. Stress-dependent finite growth in soft elastic tissues. J. Biomech. 27, 455–467.

Schmid, H., Pauli, L., Paulus, A., Kuhl, E., Itskov, M., 2011. How to utilise the kinematic constraint of incompressibility for modelling adaptation of soft tissues. Comput. Meth. Biomech. Biomed. Eng., in press. doi: 10.1080/10255842.2010.548325.

Shively, R.E., 1986. Skin expander volume estimator. Plast. Reconstr. Surg. 77, 482–483.

Silver, F.H., Siperko, L.M., Seehra, G.P., 2003. Mechanobiology of force transduction in dermal tissue. Skin Res. Technol. 9, 3–23.

Socci, L., Rennati, G., Gervaso, F., Vena, P., 2007. An axisymmetric computational model of skin expansion and growth. Biomech. Model. Mechanobiol. 6, 177–188.

Taber, L.A., 1995. Biomechanics of growth, remodeling and morphogenesis. Appl. Mech. Rev. 48, 487–545.

Taber, L.A., Humphrey, J.D., 2001. Stress-modulated growth, residual stress, and vascular heterogeneity. J. Biomech. Eng. 123, 528–535.

Takei, T., Mills, I., Arai, K., Sumpio, B.E., 1998. Molecular basis for tissue expansion: clinical implications for the surgeon. Plast. Reconstr. Surg. 102, 247–258.

Taylor, R.L., 2008. FEAP—A Finite Element Analysis Program. User Manual, Version 8.2. University of California at Berkeley.

Taylor, R.E., Zheng, C., Jackson, P.R., Doll, J.C., Chen, J.C., Holzbaur, K.R.S., Besier, T., Kuhl, E., 2009. The phenomenon of twisted growth: humeral torsion in dominant arms of high performance tennis players. Comput. Meth. Biomech. Biomed. Eng. 12, 83–93.

van der Kolk, C.A., McCann, J.J., Knight, K.R., O'Brien, B.M., 1987. Some further characteristics of expanded tissue. Clin. Plast. Surg. 14, 447–453.

Vandiver, R., Goriely, A., 2009. Differential growth and residual stress in cylindrical elastic structures. Philos. Trans. R. Soc. A 367, 3607–3630.

van Rappard, J.H.A., Molenaar, J., van Doorn, K., Sonneveld, G.J., Borghouts, J.M.H.M., 1988. Surface-area increase in tissue expansion. Plast. Reconstr. Surg. 82, 833–839.

Wollina, U., Berger, U., Stolle, C., Stolle, H., Schubert, H., Zieger, M., Hipler, C., Schumann, D., 1992. Tissue expansion in pig skin—a histochemical approach. Anat. Histol. Embryol. 21, 101–111.

Zeng, Y., Xu, C., Yang, J., Sun, G., Xu, X., 2003. Biomechanical comparison between conventional and rapid expansion of skin. Br. Assoc. Plast. Surg. 56, 660–666.